

# Supplementary Information for Bursting on a vortex tube with initial axial core-size perturbations

Lingbo Ji and Wim M. van Rees\*  
*Department of Mechanical Engineering, Massachusetts Institute of Technology, Cambridge, Massachusetts 02139, USA*

## Appendix A: Definition of the twist density $\tau(r, z) = \frac{\omega_\theta}{r\omega_z}$

To justify the definition of the twist density  $\tau(r, z) = \frac{\omega_\theta}{r\omega_z}$ , we consider a vortex line lying on the surface of an axisymmetric tube. By definition, the vorticity vector is tangent to the vortex line at each point on the line. If the core-size of the vortex tube is constant, as in Fig. 1(a), the vortex line forms a helix with pitch  $p = \frac{2\pi r\omega_z(r)}{\omega_\theta(r)}$  equal to the axial distance moved after one complete turn around the centerline. The quantity  $\tau(r) = \frac{\omega_\theta(r)}{r\omega_z(r)}$  is proportional to the inverse of the pitch of the helix at radius  $r$ , and thus serves as a measure of the degree of winding of the vortex line around the  $z$  axis. Further, for a constant core size this vortex line and the axis of the tube spans a ribbon with constant width, and  $\tau(r)$  exactly corresponds to the usual definition of twist density of a ribbon in literature [1, 2].

When considering a vortex tube with axial core-size variations, as in Fig. 1(b), each vortex line can be treated as a generalized helix centered around the  $z$  axis, with axially varying radius and pitch. In this case, evaluating  $\tau(r, z) = \frac{\omega_\theta(r, z)}{r\omega_z(r, z)}$  can be interpreted as a generalization of the twist density, equivalent to the inverse of the pitch of a local helical curve at  $(r, z)$ .

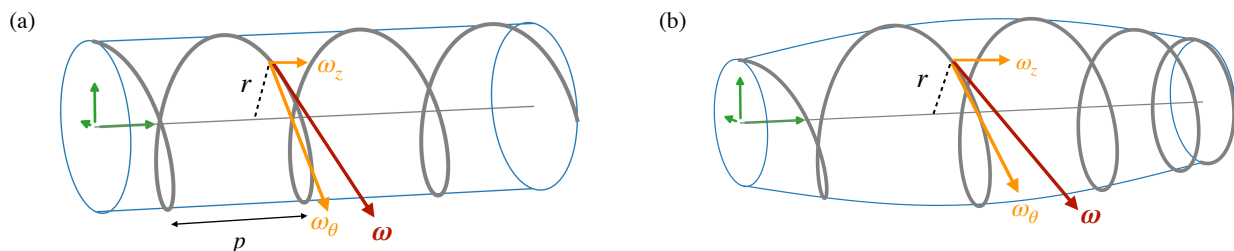


FIG. 1: Illustration of a vortex line (solid gray) lying on (a) a cylindrical vortex surface (blue) (b) an axisymmetric vortex surface with varying core size (blue). The straight centerline of the tube is shown in light gray. The green triad shows indicate coordinate system. The vorticity vector at a point which is tangent to the vortex line is indicated by a red arrow. The axial and azimuthal components, which is used in the definition of twist density  $\tau$ , are shown as orange arrows.

## Appendix B: Definition of the twist wavefront

We determine the twist wave propagation speed by tracking the position of the twist wavefront over time. In the main text the twist wavefront is defined as the axial position of maximum centerline twist density. With this definition, the twist wave speed exhibits a linear dependence on the core-size ratio  $A$  that is captured with the relation  $c/(\Gamma_0/\sigma_0) \approx 0.0620(A - 1) + 0.0616$ .

Besides the maximum centerline twist, several alternative features of the twist waves can be also be used to characterize the twist wavefront and evaluate the twist wave speed. These include:

1. A local minimum in  $\omega_z$  at the centerline is located at the twist wavefront, as shown in Fig. 2(a). This arises due to the expansion of the inner vortex core at the twist wavefront.
2. The maximum in  $|\partial u_z/\partial z|$  at the centerline is located at the twist wavefront Fig. 2(b) i.e. the axial compression is most intense at the twist wavefront. It is coupled to the local minimum in  $\omega_z$ , since at the centerline, the vorticity equation is reduced to  $\frac{\partial \omega_z}{\partial t} + u_z \frac{\partial \omega_z}{\partial z} = \omega_z \frac{\partial u_z}{\partial z}$ .

\* wvanrees@mit.edu

3. The axial position of the maximum in  $|\omega_\theta|$  in the  $r$ - $z$  plane moves with the twist wave packet.

It turns out that across all these different wavefront definitions, the twist wave propagation speed remains largely the same. This is shown in Table. I, comparing the dependency of wave propagation speed on  $A$  across the different criteria. Consequently, any of the criteria described in this section can be interchangeably used for determining the twist wave propagation speed, instead of the maximum centerline twist density described in the main text.

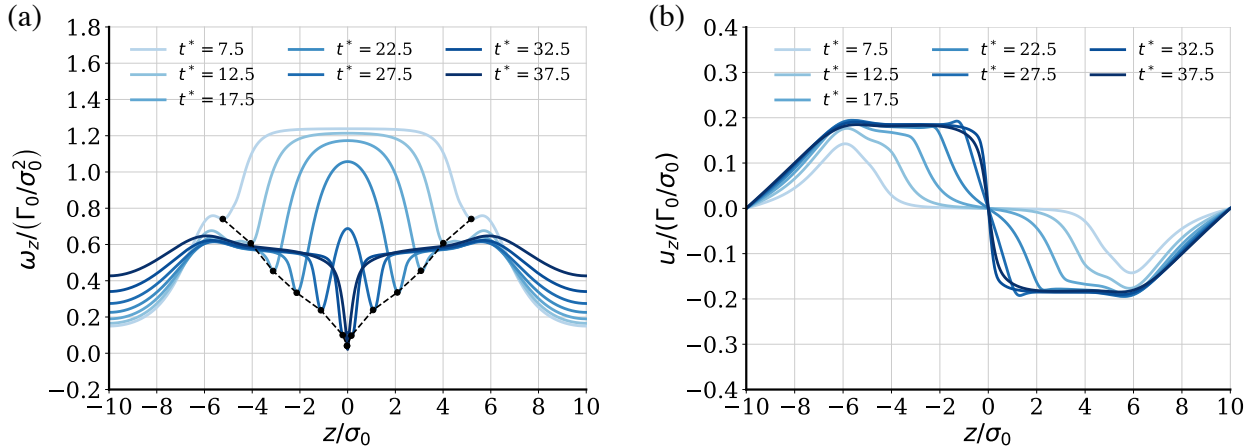


FIG. 2: (a)  $\omega_z$  and (b)  $u_z$  along centerline at selected times during the twist wave propagation for the case  $A = 3.0$ . The black dots in (a) denote the minimum value and position of  $\omega_z$ , demonstrating an approximate constant velocity of this measure of the twist wave.

Criterion for wave speed evaluation	wave speed ( $c / (\Gamma_0 / \sigma_0)$ )	square root of MSE	MAPE
$\tau_{\max}$ at centerline	$0.0620(A - 1) + 0.0616$	0.004	3.0%
$\omega_{z,\min}$ at centerline	$0.0619(A - 1) + 0.0725$	0.0013	0.89%
$ \partial u_z / \partial z _{\max}$ at centerline	$0.0607(A - 1) + 0.0656$	0.0018	1.7%
$ \omega_\theta _{\max}$ in the $r$ - $z$ plane	$0.0621(A - 1) + 0.0719$	0.0029	1.8%

TABLE I: The best linear fit functional dependency of wave speed on  $A$  evaluated using different metrics.

### Appendix C: Nonlinear wave speed based on [3]

Following Section IV in [3], we consider a vortex tube consisting of two sections with different constant core-sizes  $\sigma_1 < \sigma_2$  and suppose  $\omega_\theta = 0$  in region 1 i.e. the azimuthal circulation per unit length  $\gamma_1$  defined in [3] is zero. From Eqn. (59a) in [3], we obtain

$$c = \frac{\Gamma}{\sqrt{6}\pi} \frac{1}{\sqrt{\left(\frac{3}{4}\frac{\sigma_1^2}{\sigma_2^2} + \frac{1}{4}\right)\sigma_1^2}}. \quad (\text{C1})$$

We take  $\sigma_0 = (\sigma_1 + \sigma_2)/2$ ,  $A = \frac{\sigma_2}{\sigma_1}$ , which implies

$$c / (\Gamma_0 / \sigma_0) = \frac{1}{\sqrt{6}\pi} \frac{(1 + A)A}{\sqrt{3 + A^2}}. \quad (\text{C2})$$

For  $1 \lesssim A \leq 5.4$ , we observe that the relationship between  $c$  and  $A$  is approximately linear (Fig. 3):

$$c / (\Gamma_0 / \sigma_0) \approx 0.145(A - 1) + 0.151, \quad (\text{C3})$$

where the square root of MSE is 0.0061 and MAPE is 1.6%.

### Appendix D: Quantification of the primary bursting ring pair

To study the primary bursting ring pair, we consider the associated patch of azimuthal vorticity in the  $(r, z)$  plane, where  $e^{-1} \leq \omega_\theta / \omega_{\theta, \max} \leq 1.0$ , as shown in Fig. 4. Consistent with the description in Section V A in the main text, the ring pair grows radially outwards in the early stage of bursting.

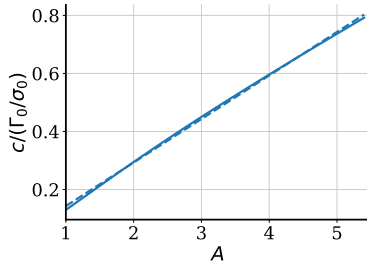


FIG. 3: The nonlinear wave speed versus  $A$  from the wave model of [3]. The solid line corresponds to Eqn. C2. The dashed line is from the linear fit (Eqn. C3).

We quantify the effective Reynolds number for the bursting ring and the ring thickness ratio at the time  $t_{\text{patch}}^*$  when the peak  $\omega_\theta$  reaches its maximum, based on the azimuthal vorticity patch shown in Fig. 4. The effective Reynolds number is  $Re_{\text{patch}} = \Gamma_{\text{patch}}/\nu$ , where the circulation  $\Gamma_{\text{patch}}$  is approximated by numerically integrating  $\omega_\theta$  over the area inside the outermost contour ( $\omega_\theta/\omega_{\theta,\text{max}} = e^{-1}$ ). The length scale of the patch  $a$  is identified as the average distance from the position of peak  $\omega_\theta$  to the points on the contour. The radius of the ring  $R$  is estimated as the radial distance of  $\omega_{\theta,\text{max}}$  from the  $z$  axis. The ring thickness is defined as  $a/R$ . The values of  $t_{\text{patch}}^*$ ,  $Re_{\text{patch}}$  and  $a/R$  are listed in Table. II.

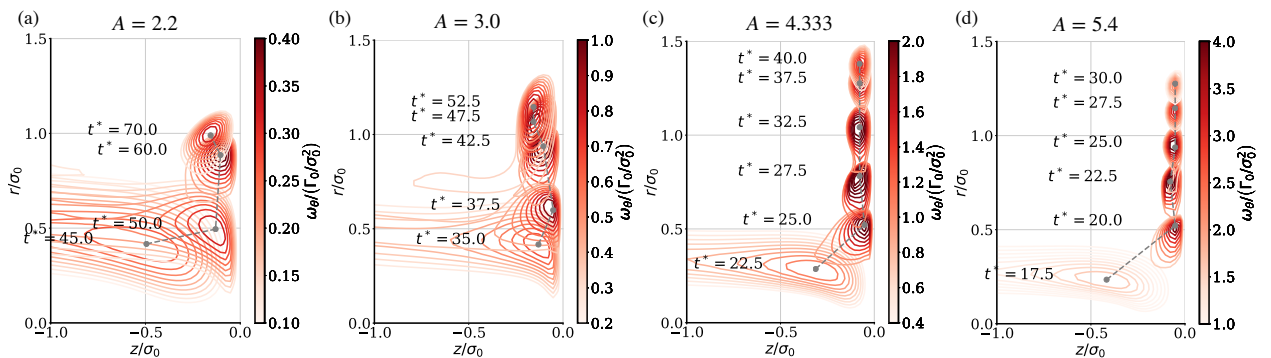


FIG. 4: The azimuthal vorticity contours of the primary bursting ring pair in the  $r$ - $z$  plane for a range of  $A$  at different times during bursting. Note the azimuthal vorticity is filtered to show only the patch of azimuthal vorticity representing the primary bursting ring pair. Only contours of  $\omega_\theta$  in the range  $e^{-1} \leq \omega_\theta/\omega_{\theta,\text{max}} \leq 1.0$  is shown for each time.

	$A = 2.2$	$A = 3.0$	$A = 4.33$	$A = 5.4$
time of evaluation $t_{\text{patch}}^*$	60.0	42.5	27.5	22.5
Effective Reynolds number $Re_{\text{patch}}$	109	232	352	379
ring thickness $a/R$	0.196	0.185	0.184	0.142

TABLE II: The effective Reynolds number  $Re_{\text{patch}} = \Gamma_{\text{patch}}/\nu$  and ring thickness (ratio of core size to ring radius  $a/R_{\text{patch}}$ ) at time  $t_{\text{patch}}^*$  for a range of values of  $A$ .

### Appendix E: Vortex bursting with non-axisymmetric initial conditions

As mentioned in the main text, we have performed a set of simulations for the case  $A = 4.333$  with initial noise in the core radius. Here the initial core-size  $\sigma(z)$  in the expressions for  $\omega_r$  and  $\omega_z$  in the main text is replaced with

$$\sigma(z, \theta) = \sigma(z) \left( 1 + \frac{A_{\text{noise}}}{2n_k} \sum_{i=1}^{n_k} (\sin(i\theta + 2\pi a_i(z)) + \cos(i\theta + 2\pi b_i(z))) \right), \quad (\text{E1})$$

where  $n_k$  is the number of azimuthal modes,  $a_i(z)$  and  $b_i(z)$  are random numbers drawn from a uniform distribution  $\mathcal{U}(0, 1)$  at each value of  $z$  and the relative amplitude of the noise is bounded by  $A_{\text{noise}}$ . Note that in Eq. (E1) the original coresize is perturbed with a noise with structure in the azimuthal direction

and not in the axial direction. The resulting nonzero divergence of this initial vorticity field is taken care through a numerical solenoidal reprojection procedure at  $t^* = 0.0$ . We consider the case  $A = 4.333$  with a noise level  $A_{\text{noise}} = 0.15$  and  $A_{\text{noise}} = 0.3$ .

In the early phase of twist wave propagation, no apparent instabilities occur in our simulated case with noise. When bursting takes place, however, an azimuthal instability develops at the bursting region, which can be observed by visualizing the  $\omega_\theta$  field (Fig. 11(d) in the main text). For the noise-free case with  $A = 4.333$ , there are two pairs of vortex ring-like structures generated in succession, which eventually merge without losing their axisymmetry. In the cases with noise, an azimuthal instability sets in at the later stages of bursting. The inner vortex ring pair exhibits deformations in both radial and axial directions, while the outer vortex ring pair decays quickly before any instabilities can be observed. The remaining second vortex ring pair oscillates, rotates and eventually breaks into finer structures, where further reconnection events take place.

Similar to the noise-free case, in the late stage of bursting twist waves of opposite signs are generated within the bursting region, which propagate away from the center plane  $z = 0$ . However, the twist waves in the cases with noise develop helical vortex structures at later times, as shown in Fig. 5 in a comparison of the vorticity field at  $t^* = 120$  for the initial condition with and without noise.

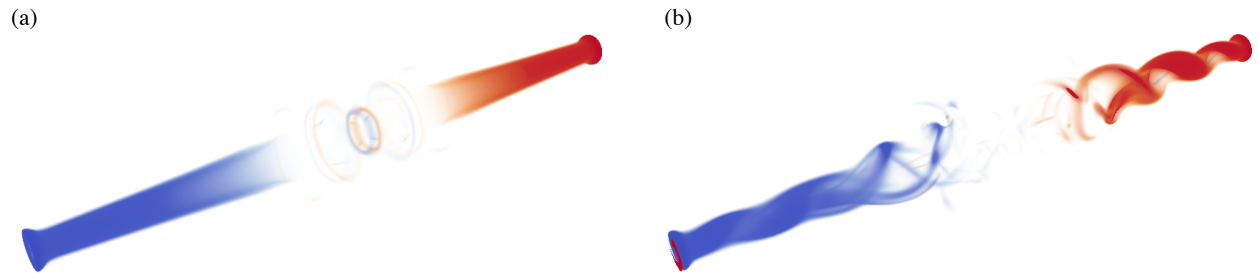


FIG. 5: Volume rendering of  $\omega_\theta$  after the first bursting at  $t^* = 120$  for the case  $A = 4.333$ , (a) without initial noise and (b) with initial noise with relative amplitude  $A_{\text{noise}} = 0.15$ . One period of the domain is visualized.

The comparison of the flow evolution can also be made by plotting the evolution of the enstrophy and energy in the domain for the unperturbed case together with the cases with two different noise amplitudes, shown in Fig. 6. Though the local instabilities discussed above do slightly affect the dynamics of bursting and subsequent flow evolution, their effect on the integral quantities of enstrophy and energy at later times is relatively limited. Consequently, our metric of the time scale of energy decay compared with an ‘equivalent’ initial unperturbed Lamb-Oseen vortex tube is very similar between the cases with and without noise, as shown in Fig. 6(b). Though these are just two instantiations of the noisy initial conditions, they indicate a robustness of the mechanisms and the global flow evolution to noise, which emphasizes the relevance of the bursting phenomenon in practical scenarios.

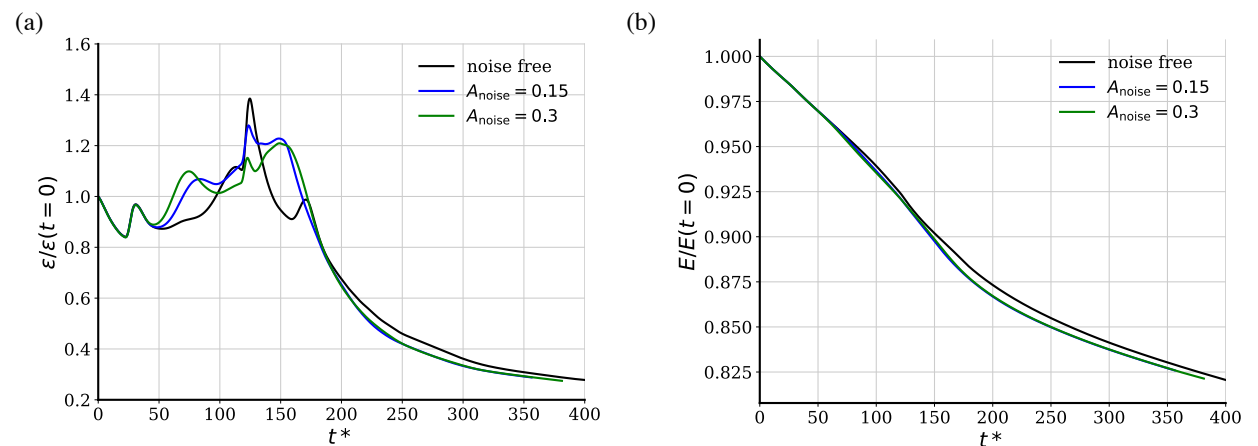


FIG. 6: The time evolution of global enstrophy for the case  $A = 4.333$  without noise (black), and two different initial noise amplitudes  $A_{\text{noise}}$  (blue and green).

## Appendix F: Radially averaged enstrophy for all values of $A$

In Fig. 7 of the main text we show the radially averaged enstrophy as a function of the axial coordinate (horizontally) and time (vertically) for  $A = 3.0$  and  $A = 4.333$ . Below we include the same plot for the entire range of values of  $A$  simulated. For  $A = 3.0$  and smaller, we observe enstrophy peaks associated with primary, secondary, and tertiary bursting events which increase as  $A$  increases (note that the colorbar scales vary across the figures). Starting at  $A = 3.571$ , we start to see diagonal streaks occurring after the second bursting event; as mentioned in the main text, these are characteristic of a helical wave instability on the vortex core itself. For  $A = 3.571$  these are not strong enough to disrupt the structure of the vortex core, and a tertiary bursting event is visible. For  $A = 4.333$  and  $A = 5.4$ , however the vortex core disintegrates into helical vortical structures which alter the qualitative evolution of the flow after the secondary bursting, and inhibit the tertiary bursting event.

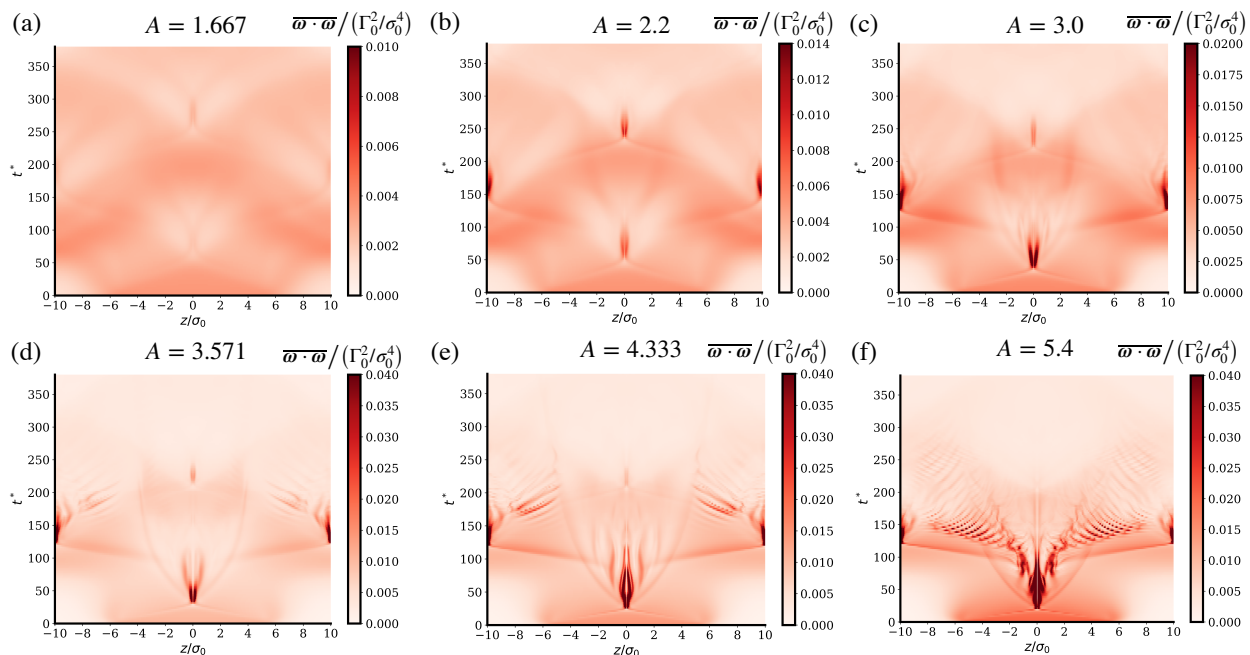


FIG. 7: Color plots of radially averaged enstrophy density  $\overline{\omega \cdot \omega} = \frac{\int \omega \cdot \omega r dr}{\int r dr}$  as a function of  $z/\sigma_0$  (horizontal axis) and non-dimensional time (vertical axis) for a range of values of  $A$ .

- 
- [1] H. K. Moffatt and R. L. Ricca, Helicity and the c alug areanu invariant, Proceedings of the Royal Society of London. Series A: Mathematical and Physical Sciences **439**, 411 (1992), <https://royalsocietypublishing.org/doi/pdf/10.1098/rspa.1992.0159>.
- [2] F. B. Fuller, The writhing number of a space curve, Proceedings of the National Academy of Sciences **68**, 815 (1971), <https://www.pnas.org/content/68/4/815.full.pdf>.
- [3] A. Leonard, Nonlocal theory of area-varying waves on axisymmetric vortex tubes, Physics of Fluids **6**, 765 (1994).